Identification of amnion progenitor-like cells at the amnion-epiblast boundary in the primate peri-gastrula

AUTHORS: Nikola Sekulovski[1], Lauren N. Juga[1], Chari L. Cortez[2], Michael Czerwinski[2,3], Allison E. Whorton[1], Jason R. Spence[2,3], Jenna K. Schmidt[4], Thaddeus G. Golos[4,5,6], Deborah L. Gumucio[2,3], Chien-Wei Lin[7] and Kenichiro Taniguchi[1,8,†]

AFFILIATIONS:
[1]Department of Cell Biology, Neurobiology and Anatomy, Medical College of Wisconsin, Milwaukee, WI 53226, USA
[2]Department of Cell and Developmental Biology, University of Michigan Medical School, Ann Arbor, MI 48109, USA
[3]Department of Internal Medicine, University of Michigan Medical School, Ann Arbor, MI 48109, USA
[4]Wisconsin National Primate Research Center (WNPRC), Madison, WI, USA
[5]Department of Obstetrics and Gynecology, University of Wisconsin - Madison School of Medicine, Madison, WI USA
[6]Department of Comparative Biosciences, University of Wisconsin - Madison School of Veterinary Medicine, Madison, WI, USA
[7]Division of Biostatistics, Medical College of Wisconsin, Milwaukee, WI 53226, USA
[8]Department of Pediatrics, Medical College of Wisconsin, Milwaukee, WI 53226, USA

[†]Corresponding author

CONTACTS:
Kenichiro Taniguchi
8701 Watertown Plank Road
B4245 BSB CB062
Milwaukee, WI 53226
ktaniguchi@mcw.edu

ABSTRACT

Amniogenesis is triggered in a collection of pluripotent epiblast cells as the human embryo implants. To gain insights into the critical but poorly understood transcriptional machinery governing amnion fate determination, we examined the evolving transcriptome of a developing human pluripotent stem cell-derived amnion model at the single cell level. This analysis revealed a previously unrecognized CLDN10^{+} amnion progenitor cell type and enabled the identification of several markers specific to the different stages of lineage progression. Strikingly, we found that expression of CLDN10 is restricted to the amnion-epiblast boundary region in peri-gastrula cynomolgus macaque embryos, bolstering the notion that, at this stage, the amnion-epiblast boundary is a site of active amniogenesis. Bioinformatic analysis of published primate peri-gastrula single cell sequencing data further confirmed that CLDN10 is expressed in cells progressing to amnion. Overall, this study identifies a previously unrecognized CLDN10^{+} amnion progenitor-like cell population and validates the presence of these fate transitioning cells at the boundary of the developing amnion.

INTRODUCTION

Amniogenesis is a critical event that is initiated during implantation in humans, eventually leading to the formation of an amniotic sac structure that surrounds and protects the developing embryo (Enders et al., 1983; Enders et al., 1986; Miki et al., 2005; Sasaki et al., 2016; Shahbazi and Zernicka-Goetz, 2018; Taniguchi et al., 2019). At implantation, the embryo (referred to at this time as a blastocyst) contains three morphologically and molecularly distinct cell types: a collection of unpolarized pluripotent epiblast cells (precursors to both the embryo proper and the amniotic ectoderm), a surrounding layer of polarized trophectoderm (a placental tissue precursor) and an underlying extraembryonic primitive endoderm (a yolk sac precursor). Upon implantation, the pluripotent epiblast cells undergo apico-basal polarization to form a cyst with a central lumen, the future amniotic cavity (Carleton et al., 2022). This event is followed by the fate transition of pluripotent epiblast cells at the uterine-proximal pole of the cyst to squamous amniotic ectoderm, forming a sharp boundary between amnion and pluripotent epiblast portions of the cyst (Shahbazi and Zernicka-Goetz, 2018; Shao and Fu, 2022; Taniguchi et al., 2019). This structure, known as the amniotic sac, represents the substrate for the next essential steps of embryonic development (e.g., primitive streak formation, neural specification).

Recent studies using early human and monkey embryos have provided a basic understanding of the transcriptomic characteristics of early primate amniogenesis (Bergmann et al., 2022; Nakamura et al., 2016; Nakamura et al., 2017; Sasaki et al., 2016; Tyser et al., 2021; Yang et al., 2021). Yet, experimental dissection of the molecular mechanisms involved in this process is difficult in these *in vivo* models. To enable molecular and cellular investigations, we and others developed human pluripotent stem cell-derived amnion models and showed that BMP signaling plays a crucial role in initiating amniogenesis (Chen et al., 2021; Overeem et al., 2023; Shao et al., 2017a; Shao et al., 2017b; Zheng et al., 2019). Recently, we further explored the BMP-dependent amniogenic transcriptional cascade, identifying several distinct transcriptional stages, as well as a requirement for TFAP2A-dependent transcription in regulating amnion fate progression (Sekulovski et al., 2023). However, changes in cellular differentiation states during amnion lineage progression remain largely unexplored.

In this study, we used single cell RNA sequencing (scRNA-seq) analysis to examine the dynamics in gene expression that accompany amnion differentiation of hPSC (herein referred to as the hPSC-amnion) cultured in a soft gel environment, called Gel-3D (Shao et al., 2017a). In this Gel-3D amnion model, BMP signaling, activated by a mechanosensitive cue provided by the soft substrate, is a critical initiator of human amniogenesis (Shao and Fu, 2022; Shao et al., 2017a; Taniguchi et al., 2019). Interestingly, the data reveal two likely contiguous amniogenic cell states: an amnion progenitor (AmP) state as well as an advanced amnion (advAm) state, each of which shows transcriptional similarities to distinct cell types in a Carnegie stage 7 human embryo (Tyser et al., 2021). Importantly, we identify a cohort of markers specific to each of these two amnion states, and validate selected markers for their expression in the amnion from cynomolgus macaque (*Macaca fascicularis*) embryos. Strikingly, we show that CLDN10, a marker of the AmP population, exhibits a restricted amniotic expression pattern at the boundary between the amnion and the epiblast of the cynomolgus

macaque peri-gastrula. This further supports our findings from a separate study (Sekulovski et al., 2023), which show that the amnion-epiblast boundary is a site of active amniogenesis in the macaque peri-gastrula. Together, this study provides important single cell-level insight into human amnion fate progression and presents additional evidence for the presence of amnion progenitor-like cells in primate embryos undergoing gastrulation.

RESULTS AND DISCUSSION

Previously, we described culture conditions (Gel-3D) in which plated hPSC form polarized cysts initially composed of columnar pluripotent cells, which then spontaneously undergo squamous morphogenesis and begin to express amnion markers (Shao et al., 2017a). Specifically, singly dissociated hPSC are plated densely on a soft gel substrate to form aggregates and are allowed to grow for 24 hours (hrs) in the presence of a ROCK inhibitor (Y-27632). After the first 24 hrs (day 1, d1), the ROCK inhibitor is removed (a trigger to initiate lumenal cyst formation (Hamed et al., 2023; Shao et al., 2017a; Taniguchi et al., 2015)), and a diluted extracellular matrix gel overlay (2% v/v, e.g., Geltrex) is added to provide an additional 3D cue. Immunofluorescent (IF) staining at this time shows cuboidal cells surrounding a central lumen; these cells express NANOG, but not TFAP2A (**Fig. 1A**).

Interestingly, 24 hrs after adding the gel overlay (d2), a subset of cells within the cysts display reduced expression of NANOG and SOX2, while TFAP2A expression becomes weakly activated (**Fig. 1A**, arrowhead in d2). By d3, NANOG is no longer detectable. Moreover, while many cells exhibit prominent TFAP2A expression, some cells are only weakly positive for TFAP2A (**Fig. 1A**, arrowheads). This pattern of TFAP2A expression is consistent with the previous observation that amniogenesis initiates focally on the pluripotent cysts and then spreads laterally to form fully squamous cysts (**Fig. 1A**, (Shao et al., 2017a; Shao et al., 2017b)). These molecular changes are accompanied by a decrease in nuclear aspect ratio (a measure of epithelial cell morphology, (Shao et al., 2017a; Townshend et al., 2020)) over time, revealing more flattened (squamous) shapes by d3 and d4 (**Fig. 1B**). These results provide further molecular and structural evidence that the transition from pluripotent to amnion cell types occurs progressively over the cyst, starting from focal initiation sites (Shao et al., 2017a; Shao et al., 2017b). As expected for such a spreading fate conversion, d2 and d3 cysts contain cells representing several differentiation states.

To explore transcriptional programs of the fate transitioning cells during early stages of human amnion development in this model, we performed scRNA-seq analysis of d3 hPSC-amnion cysts, in which molecularly distinct amniotic cell types co-exist within same cyst (**Fig. 1A**, d3). d3 hPSC-amnion cysts were dissociated into single cells, followed by single cell isolation and labeling using the Fluidigm C3 system, cDNA amplification and sequencing followed by demultiplexing (see Material and Methods for additional details). This scRNA-seq dataset was examined using Seurat (Butler et al., 2018) for data filtering, regression for genes associated with cell cycle progression, normalization, variable gene selection and subsequent unsupervised clustering of cells (see Materials and Methods). The data yield two distinct populations among 379 cells, which, after marker and lineage analyses described below, are labeled AmP (amnion progenitor, sage color) and advAm (advanced amnion, salmon color). Transcriptomic

features of these cells are visualized in Uniform Manifold Approximation and Projection (UMAP) plots (**Fig. 1C**). Analysis of cell cycle markers reveals that cells of the AmP population are predominantly in S phase, while in advAm cells, G1 phase markers predominate (**Fig. S1**).

To broadly characterize the transcriptional state of each population, we examined the expression of known amnion markers (Roost et al., 2015; Shao et al., 2017a; Yang et al., 2021; Zhao et al., 2021; Zheng et al., 2022). Consistent with the amniotic lineage, *pan*-amnion markers (*ISL1*, *TFAP2A* and *GATA3*, **Fig. 1D**, expression superimposed on the UMAP plot in **Fig. 1C**) are expressed in cells of both populations. In contrast, *GABRP*, *VTCN*1 and *IGFBP3* – differentiated amnion markers expressed in the first-trimester human amnion (Roost et al., 2015) and detected in other human amnion models (Shao et al., 2017a; Yang et al., 2021; Zhao et al., 2021; Zheng et al., 2022) – are enriched primarily in salmon-colored cells (**Fig. 1E**), indicating that this population contains cells characteristic of more advanced amnion states (advAm). Indeed, pseudotime analysis (Cao et al., 2019) identifies distinct changes in gene expression dynamics within the cell population, with cells on the left side of the plot showing characteristics of less mature cells and those on the right side exhibiting more differentiated profiles (**Fig. 1F**). In agreement with this idea, when RNA-velocity analysis (velocyto, (La Manno et al., 2018)) was applied to examine lineage relationships among the two populations based on the relative abundance of unspliced and spliced mRNA in each cell, the majority of the RNA vector trajectories were directed toward advAm cells on the right side of the plot (**Fig. 1G**, RNA velocity superimposed on the UMAP plot). These results suggest that the cells marked in sage color in **Fig. 1C**, which do not express later amnion markers, may be previously unrecognized precursor cell types (AmP) that give rise to more mature amniotic cells.

In a recent study, we performed a detailed meta-analysis of the Tyser *et al.* scRNA-seq dataset from a human embryo staged at Carnegie stage 7 (CS7) (Tyser et al., 2021) and showed that the rod-shaped cluster of cells annotated as “Ectoderm” is comprised of lineage progressing, lineage committed, and fully differentiated amnion cell types (Sekulovski et al., 2023). The Tyser *et al*. UMAP plot is reproduced in **Fig. 1H** with the original coordinates and annotations. Here, we show that *pan*-amnion markers such as *GATA3, TFAP2A and ISL1* are broadly expressed in the rod-shaped cell population marked “Ectoderm” (reproduced in **Fig. 1I**, see **Fig. S2** for uncropped expression plots). Cells expressing the advAm markers, *GABRP*, *VTCN*1 and *IGFBP3*, are found at the distal tip of this rod-shaped Ectoderm population (**Fig. 1J**). To examine which cells in the CS7 human embryo share transcriptomic similarities to AmP or advAm cells, the scRNA-seq dataset from the Tyser *et al.* CS7 human embryo was combined with our d3 hPSC-amnion model and normalized using an integration feature based on canonical correlation analysis in Seurat (Hao et al., 2021) (**Fig. 1K-M**). Though the combined UMAP plot of this integrated dataset is different in shape from the original Tyser *et al.* UMAP, it is clear that the cells from our d3 hPSC-amnion dataset map to the regions marked by Tyser *et al*. as Epiblast, Primitive Streak and Ectoderm. Moreover, while AmP cells are populated across the Tyser Epiblast and Primitive Streak clusters, advAm cells overlap substantially with Tyser Ectoderm cells (**Fig. 1L,M**), further validating the human amnion-like transcriptional characteristics of Gel-3D amnion models (expression of selected markers shown in **Fig. S3**). Together, these

184 results strongly support our notion that AmP markers characterize a progenitor-like cell
185 population with transcriptional features that are more similar to pluripotent and primitive
186 streak cell types, and that further differentiated amnion cells can be identified using
187 advAm markers.
188 To identify genes that are unique to each cluster, unsupervised differential gene
189 enrichment analysis was performed (**Table 1**, $p < 0.05$, selected advAm cluster markers
190 shown in **Fig. 2A**). As expected, the advAm cluster shows enriched expression of
191 additional known differentiated amnion markers (e.g., *HIF-2A/EPAS1*, *IGFBP3, GABRP*)
192 as well as previously uncharacterized genes (**Table 1**, e.g., *ADAMTS18* and *SESN3*).
193 To confirm these findings in an *in vivo* system, we used RNA *in situ* hybridization to
194 examine the amniotic expression of selected differentiated markers (*GABRP*,
195 *ADAMTS18* and *SESN3*, co-stained for *ISL1*) in a cynomolgus macaque (*Macaca*
196 *fascicularis*) embryo staged between Carnegie stages (CS) 12 and 13, an
197 organogenesis stage (**Fig. 2B,C**). Expression of all three markers is observed in the
198 amnion of this embryo, supporting the conclusion that the markers found in advAm cells
199 are valid markers of differentiated amnion. Interestingly, while *GABRP* and *SESN3*
200 show expression throughout the amnion, *ADAMTS18* expression is restricted to a
201 fraction of cells within the amnion (**Fig. 2C**), perhaps labeling a previously unrecognized
202 amnion sub-population.
203 The differential gene enrichment analysis also revealed that the AmP cells
204 (marked in sage in **Fig. 1C**) exhibit high expression of genes including *FABP5*, *IFITM1*
205 and *CLDN10* (**Fig. 3A** (dotplot), **3B** (UMAP)). Among these markers, only *CLDN10* (a
206 gene encoding Claudin-10, a component of tight junction) shows an enriched
207 expression in the "Primitive Streak" cells directly adjacent to the "Ectoderm" cells in the
208 Tyser *et al.* UMAP (**Fig. 3B**, uncropped image in **Fig. S4A**); we previously showed that
209 this subpopulation of the Primitive Streak cells displays weak *TBXT* expression, and
210 appears to include intermediate cells transitioning to amnion (Sekulovski et al., 2023), a
211 notion supported by a recent species comparison study by others (Ton et al., 2023). A
212 similar *TBXT* expression pattern is seen in a scRNA-seq dataset from d14 cynomolgus
213 macaque peri-gastrula (**Fig. S4B,C**, (Yang et al., 2021)). Indeed, CLDN10 enriched
214 cells are also seen within the *TBXT*^{low} cell population in the d14 cynomolgus macaque
215 embryos (**Fig. S4C**), suggesting that CLDN10^{+} progenitor cells might play a role in
216 amniogenesis at earlier timepoints.
217 Using IF staining in our hPSC-amnion model, we validated a dynamic expression
218 pattern of CLDN10 over time (**Fig. 3C**). In d2 hPSC-amnion cysts, CLDN10 expression
219 is restricted to the small fraction of cells that are weakly positive for TFAP2A (**Fig. 3C**,
220 arrowhead). At d3, CLDN10 is co-expressed with TFAP2A in several, but not all cells. In
221 contrast, most cells at d4 retain abundant TFAP2A expression but do not express
222 CLDN10 (**Fig. 3C**). Importantly, our analysis for nuclear aspect ratio (NAR) shows that,
223 at d2, CLDN10^{+} cells (NAR = 0.54 ± 0.17 STDEV, n = 39) are significantly more
224 squamous compared to CLDN10^{-} cells (NAR = 0.97 ± 0.31 STDEV, n = 87, $p<0.001$).
225 While previous studies implicated *CLDN10* as an amnion marker (Zheng et al., 2019;
226 Zheng et al., 2022), a detailed analysis was not performed. Thus, these data present
227 evidence suggesting that CLDN10 marks an early amnion state, but its expression is
228 extinguished in more differentiated cells. Consistent with this result, CLDN10 displays a

229 similar transient expression pattern in a newly established Glass-3D^{+BMP} hPSC-amnion
230 model (Sekulovski et al., 2023).
231 Interestingly, in PASE (post-implantation amniotic sac embryoids), an *in vitro*
232 model of human amniotic sac formation (Shao et al., 2017b), CLDN10 is localized
233 specifically to cells at the boundary between squamous amnion and columnar
234 pluripotent cells (**Fig. 3D**, arrowheads), an intriguing finding which suggests that cells
235 with a unique progenitor-like state might be present in the developing primate amniotic
236 sac *in vivo*. To test this, we analyzed CLDN10 expression in two cynomolgus macaque
237 embryos displaying the amniotic sac (**Fig. 3E**, staged between CS6 and CS7; **Fig. 3F**,
238 staged at CS7). Strikingly, both show restricted expression of CLDN10 at the boundary
239 separating amnion and epiblast tissues. These results are consistent with our recent
240 findings indicating that this boundary is likely a site of active amniogenesis in the
241 primate peri-gastrula (Sekulovski et al., 2023). Importantly, cynomolgus macaque
242 embryos from later stages (**Fig. 4A,B**, CS8; **Fig. 4C,D**, CS9) also show CLDN10
243 positive cells at the amnion-embryo boundary. In the CS8 embryo, CLDN10^{+} cells are
244 seen at the tip of the head fold, a region spanning the anterior most neuroectoderm and
245 the nascent mediolateral surface ectoderm (**Fig. 4A,B** – inset (ii)) as well as the
246 posterior region of the embryo-amnion boundary (**Fig. 4A,B** – inset (i)). Moreover, in the
247 CS9 embryo, while a collection of cells expressing weak CLDN10 is seen posteriorly
248 (**Fig. 4C,D** – inset (iii)), CLDN10 expression is highly prominent anteriorly in the cells at
249 the boundary of the amnion and the developing mediolateral placode (**Fig. 4C,D** – inset
250 (i)). Together, these results establish the presence of previously unrecognized CLDN10^{+}
251 amnion-embryo boundary population during gastrulation as well as during early
252 organogenesis in the cynomolgus macaque.
253 In summary, we have profiled the transcriptomic signatures of lineage
254 progressing cells in an *in vitro* model of hPSC-amnion development at the single cell
255 level. Key results were validated *in vivo*, using early monkey embryo sections and two
256 published single cell RNA sequencing datasets from early human and cynomolgus
257 macaque embryos (Tyser et al., 2021; Yang et al., 2021). These analyses reveal a
258 previously unrecognized CLDN10^{+} amnion progenitor-like cell population that is
259 localized at the boundary between the amnion and the epiblast of the amniotic sac in
260 cynomolgus macaque peri-gastrula. Strikingly, our recent study (Sekulovski et al., 2023)
261 provided evidence for an active amniogenic transcriptional cascade at the
262 epiblast/amnion boundary in primate peri-gastrula embryos; this present work reveals
263 CLDN10 as a key marker for this boundary cell population. Given the role of Claudin
264 proteins in controlling tight junction properties and epithelial characteristics (Angelow et
265 al., 2008), CLDN10 might be critical for organizing the boundary structure containing
266 shape/fate-transitioning cells flanked by squamous amnion or columnar/pseudostratified
267 pluripotent cells at each end. Molecularly, we speculate that the polarized distribution of
268 CLDN10 expression, which varies across embryo stages, might be linked to active BMP
269 signaling in each vicinity. We have previously shown that PASE are posteriorlized and
270 display high BMP signaling output (Shao et al., 2017b). At CS7, anterior BMP signaling
271 is likely inhibited by secreted BMP antagonists (e.g., Chordin, Noggin) derived from the
272 axial mesendoderm, while the posterior boundary is in close proximity to the primitive
273 streak with active BMP signaling (Anderson et al., 2002; Arnold and Robertson, 2009;
274 Shawlot et al., 1999; Yang et al., 2010). At CS8, CLDN10 appears to increase

anteriorly, perhaps due to increased BMP signaling output as the forebrain tissue expands anteriorly away from the midline tissue (e.g., prechordal plate) that secretes BMP antagonists (Anderson et al., 2002; Dobreva et al., 2012; Geng and Oliver, 2009; Muenke and Beachy, 2000; Nishioka et al., 2005). By CS9, BMP signaling output may weaken in the extending primitive streak, while strengthening anteriorly as BMP levels in this region increase (Dobreva et al., 2012). Further analyses of dynamic BMP signaling gradients will be required to test these hypotheses. Together, this study provides an important single cell transcriptomic resource for future investigation of the amniogenic transcriptional cascade in developing primate embryos.

MATERIALS AND METHODS

hESC lines

Human embryonic stem cell line H9 was used in this study (WA09, P30, P48, WiCell; NIH registration number: 0062). All protocols for the use of hPSC lines were approved by the Human Stem Cell Research Oversight Committee at the Medical College of Wisconsin and the Human Pluripotent Stem Cell Research Oversight Committee at the University of Michigan. All hPSC lines were maintained in a feeder-free system for at least 20 passages and authenticated as karyotypically normal at the indicated passage number. Karyotype analysis was performed at Cell Line Genetics. All hPSC lines tested negative for mycoplasma contamination (LookOut Mycoplasma PCR Detection Kit, Sigma-Aldrich). In summary, hESC were maintained in a feeder-free culture system with mTeSR1 medium, or with 50%/50% mix of mTeSR1 and mTeSR plus (STEMCELL Technologies). hESC were cultured on 1% (v/v) Geltrex (Thermo Fisher Scientific), or with Cultrex SCQ (Bio-techne) coated 6 well plates (Nunc). Cells were passaged as small clumps every 4 to 5 days with Dispase (Gibco). All cells were cultured at 37°C with 5% CO_2. Media was changed every day. hESC were visually checked every day to ensure the absence of spontaneously differentiated, mesenchyme-like cells in the culture. Minor differentiated cells were scratched off the plate under a dissecting scope once identified. The quality of all hESC lines was periodically examined by immunostaining for pluripotency markers and successful differentiation to three germ layer cells.

Gel-3D hPSC-amnion formation assays

Methods for these assays have been previously described (Shao et al., 2017a; Shao et al., 2017b) with exceptions that 60-70uL of undiluted ECM gel solution is hand-streaked on ice cold 22mmx22mm square coverslips, and that, in addition to Geltrex (Life Technologies), Cultrex Ultimatrix (Bio-Techne) was also used. Singly dissociated cells were prepared using Accutase (Sigma-Aldrich) and were plated on ECM gel-coated coverslips at 25,000 cells/cm^2 in mTeSR1 or in 50%/50% mTeSR1/mTeSR plus mix medium in the presence of 10μM Y-27632 (STEMCELL Technologies). After 24 hr, cells were then incubated in media containing 2% Geltrex/Ultimatrix overlay without Y-27632 with daily media changes (note that 1% gel overlay was used between d2 to d4).

Cynomolgus macaque

Animals

The female and male cynomolgus macaques were housed and cared for at the Wisconsin National Primate Research Center (WNPRC). All procedures were performed in accordance with the NIH Guide for the Care and Use of Laboratory Animals and under approval of the University of Wisconsin College of Letters and Sciences and Vice Chancellor Office for Research and Graduate Education Institutional Animal Care and Use Committee (protocol g005061).

Animal breeding and pregnancy detection

Beginning on day 8 post-onset of menses, the female was housed with a compatible male and monitored for breeding. Animals were pair-housed until day 16-20 post-onset of menses. A 2-3 mL blood draw was performed daily from day 8 post-onset of menses until day 16 to assess the timing of ovulation based on the estradiol peak and rise in progesterone in serum. Serum samples were analyzed for estradiol (25 μL) and progesterone (20 μL) using a cobas e411 analyzer equipped with ElectroChemiLuminescence technology (Roche, Basal, Switzerland) according to manufacturer instructions. Results were determined via a calibration curve which was instrument-generated by 2-point calibration using traceable standards and a master curve provided via the reagent barcode. Inter-assay coefficient of variation (CV) was determined by assaying aliquots of a pool of rhesus plasma. For estradiol, the limit of quantitation (LOQ) was 25 pg/mL, the intra-assay CV was 2.02%, and the inter-assay CV was 5.05%. For progesterone, the LOQ was 0.2 ng/mL, the intra-assay CV was 1.37%, and the inter-assay CV was 4.63%. A transabdominal ultrasound was performed to detect pregnancy as early as 14 days post-ovulation. The ultrasound measurements in combination with the timing of ovulation were used to estimate the day of conception and gestational age of the pregnancy.

Terminal perfusion uterine collection, paraffin embedding, sectioning and staining

The pregnant females were sedated with intramuscular ketamine (>15 mg/kg) followed by IV sodium pentobarbital (>35 mg/kg) and then perfused with 4% paraformaldehyde (PFA) via the left ventricle. The entire uterus and cervix were removed. The serosa and superficial myometrium were scored for better fixative penetration and to denote dorsal and ventral orientation. Tissues were fixed in 4% PFA with constant stirring and solution changes were performed every 24 hrs for a total of 72 hrs. The uterus was serially sectioned from the fundus to the internal cervical os into 4 mm slices using a dissection box. Cassettes with tissue sections were transferred into 70% ethanol, routinely processed in an automated tissue processor and embedded in paraffin for histological analyses (5 μm sections). Fixed uterine tissue were cut in 5 μm thick cross-sections, mounted on slides, deparaffinized in xylene and rehydrated in an ethanol series. Antigen retrieval was performed by boiling in citrate buffer. Sections were blocked 4% goat serum in PBS at RT for at least 3-hr. Subsequent immunolocalization was performed using commercially available primary antibodies, incubated overnight at 4 °C in 4% serum. Immunofluorescent detection was performed using secondary antibodies tagged with a fluorescent dye (fluorophores excitation = 488, 555, and 647nm), and counterstained with DAPI. Negative controls were performed in which the primary antibody was substituted with the same concentration of normal IgG of the appropriate isotype. Images were obtained with a Zeiss LSM980 microscope.

366
367 *Confocal microscopy of fixed samples*
368 Confocal Images of fixed samples were acquired using a Nikon-A1 (Nikon) and a Zeiss
369 LS980 laser scanning confocal microscopes. Non-3D images were generated using
370 Zen, FIJI (NIH) and Photoshop (Adobe).
371
372 *Immunostaining*
373 hPSC-amnion cysts grown on the coverslip were rinsed with PBS (Gibco) twice, fixed
374 with 4% paraformaldehyde (Sigma) for 60 min, then rinsed with PBS three times, and
375 permeabilized with 0.1% SDS (Sigma, in 1x PBS) solution for 60 min. The samples
376 were blocked in 4% heat-inactivated goat serum (Gibco) or 4% normal donkey serum
377 (Gibco) in PBS overnight at 4°C. The samples were incubated with primary antibody
378 solution prepared in blocking solution at 4°C for 48 hr, washed three times with PBS (30
379 min each), and incubated in blocking solution with goat or donkey raised Alexa Fluor-
380 conjugated secondary antibodies (Thermo Fisher), at room temperature for 24 hours.
381 Counter staining was performed using Hoechst 33342 (nucleus, Thermo Fisher
382 Scientific), Alexa-Fluor-conjugated wheat germ agglutinin (membrane, Thermo Fisher
383 Scientific) and Phalloidin (F-ACTIN, Thermo Fisher). All samples were mounted on
384 slides using 90% glycerol (in 1x PBS). When mounting hPSC-cysts samples, modeling
385 clay was used as a spacer between coverslip and slide to preserve lumenal cyst
386 morphology. Antibodies for IF staining are found in **Table S2**.
387
388 *RNA isolation and labeling*
389 *Single cell RNA sequencing*
390 hPSC-amnion samples were rinsed twice with DMEM/F12, were briefly treated with
391 0.05% Trypsin (Life Technologies) for 1.5-min to initiate ECM gel digestion and were
392 rinsed twice with DMEM/F12. Subsequently, the samples were incubated with Accutase
393 (Sigma) for 10-min and were dissociated into single cells by gentle agitation. The
394 scRNA-seq samples were prepared in the University of Michigan Rogel Cancer Center
395 Single Cell Analysis Core. Cells were spun down for 5-min at 300xg, and the cell pellet
396 was resuspended for Fluidigm C1 analysis (single cell preparation, single cell isolation
397 and barcoding performed according to the manufacture's instructions). Libraries were
398 sequenced (Illumina HiSeq 4000 H4K paired-end 150 cycle) followed by quality control
399 (adaptor trimming, de-duplication), alignment and demultiplexing based on
400 manufactured indices.
401
402 *Bioinformatics – single cell RNA sequencing dataset analysis*
403 Analysis of the d3 amnion scRNA-seq dataset was performed using the Seurat R
404 package (v.4.2.1, (Hao et al., 2021)). Cells were filtered out if the total number of
405 detected genes was less than 2,600 or if the expression percentage from mitochondrial
406 genes was greater than 15%. Expression values were then log-normalized with scaling
407 factor 10,000 for cell-level normalization, and further centered and scaled across genes.
408 Principal component analysis (PCA) with top 30 PCs was performed prior to embedding
409 379 cells into two dimensional space with UMAP. Cell clusters were identified using
410 FindClusters function based on a shared nearest neighbor modularity optimization

clustering algorithm (resolution set as 1). The cluster marker genes were identified using FindAllMarkers function (Wilcoxon Rank Sum test).

Mapping and gene expression analyses of Tyser et al. Carnegie Stage 7 human embryo single cell RNA sequencing dataset

The original UMAP coordinates and annotations for all 1,195 cells were used in **Fig. 1H** as well as in the accompanying expression plots. The processed data were downloaded from http://www.human-gastrula.net, which was used to generate a UMAP plot (using DimPlot function in R package Seurat), as well as to perform expression analyses (FeaturePlot function in Seurat).

Integration and gene expression analyses of d3 amnion and Tyser et al. Carnegie Stage 7 human embryo single cell RNA sequencing datasets

The two single cell datasets were integrated using a canonical correlation analysis based approach implemented in the IntegrateData function with 4,000 anchor features and 20 dimensions for anchor weighting in Seurat R package (v4.2.1).

Integration and gene expression analyses of Yang et al. GD14 cynomolgus macaque embryo single cell RNA sequencing dataset

The processed data were downloaded from GSE148683, and the ensemble genome build Macaca_fascicularis_5.0 release 96 was used to identify human orthogonal gene symbols. Datasets from two distinct GD14 embryos (Yang et al., 2021) were integrated using 5,000 anchor features and 10 dimensions in the IntegrateData function in Seurat R package (v.4.2.1) package. Six general cell populations (epiblast, transition, mesoderm, amnion, endoderm and extraembryonic mesenchyme) were identified using FindClusters function (resolution as 0.4).

Pseudotime

Pseudotime analysis was performed using R package Monocle 3 (Cao et al., 2019). UMAP was used to learn the principal graph using reverse graph embedding algorithm. To decide the start of the trajectory, given that we defined that AmP is the initial lineage in this dataset, we selected the node with the lowest value of the first UMAP component as the root node. The estimated pseudotime was overlayed onto the original UMAP coordinates.

RNA velocity (velocyto) analysis

After alignment to human genome hg19, the BAM files were used to generate a loom file using the function run_smartseq2 in Python package velocyto (v0.17) with default parameters to create spliced and unspliced gene count matrices. R package velocyto.R (Python package v.0.6 (Bergen et al., 2020) was used to estimate inferred RNA velocities of single cells and we visualized the velocities on the original UMAP embedding.

FIGURES AND FIGURE LEGENDS

Figure 1. Single-cell transcriptomic signatures of d3 human amnion model

(A) Confocal images of d1, d2, d3 and d4 hPSC-amnion cysts stained for TFAP2A, an amnion marker, and NANOG, a pluripotency marker. White arrowheads indicate cells that display weak TFAP2A expression. Scale bars = 20μm.
(B) Quantitation for nuclear aspect ratio, a measure of epithelial cell morphology, of developing hPSC-amnion at indicated timepoints, revealing a gradual squamous morphogenesis. * indicates $p < 0.05$.
(C) A UMAP plot displaying the single cell transcriptomes of 379 d3 hPSC-amnion cells with two identified clusters (AmP – sage color; advAm – salmon color).
(D,E) Expression of *pan*-amnion (*ISL1*, *TFAP2A* and *GATA3*) as well as late/advanced amnion (*GABRP*, *VTCN1*, *IGFBP3*) markers superimposed onto the UMAP plot.
(F) Pseudotime progression (Monocle 3, indicated by the gradient scale) is superimposed onto the UMAP plot.
(G) RNA velocity analysis (velocyto) of the d3 hPSC-amnion dataset, showing predicted lineage progression trajectories from AmP (left) to advAm (right) populations.
(H) A UMAP plot displaying the original single cell transcriptome coordinates of the CS7 human embryo described in Tyser *et al.*, shown with the original annotations. The inset (**i**) is used for expression analyses in (I) and (J).
(I,J) Expression of *pan*-amnion (*ISL1*, *TFAP2A* and *GATA3*) as well as late/advanced amnion (*GABRP*, *VTCN1*, *IGFBP3*) markers, superimposed onto the Tyser *et al.* UMAP plot.
(K-M) A UMAP plot showing the integrated single cell transcriptomes of d3 hPSC-amnion and Tyser *et al.* CS7 embryo datasets, revealing close overlap of hPSC-amnion cells with Tyser Epiblast, Primitive Streak and Ectoderm/Amnion cells (shown in (L) with annotations in Tyser *et al.*, magnified in (M); AmP and advAm coloring is identical to (C)). Note that a small number of hPSC-amnion cells show an overlap with Advanced Mesoderm cells, possibly due to cardiac differentiation triggered by high BMP input.

Figure 2. Validation of selected advAm markers in a cynomolgus macaque embryo staged between CS12 and CS13

(A) A dotplot of selected known and previously unrecognized late/advanced amnion markers.
(B,C) CS12/13 cynomolgus macaque embryo sections were stained for indicated markers (B: *GABRP* – green, *SESN3* – red, *ISL1* – magenta; C: *ADAMTS18* – green, *SESN3* – red, *ISL1* – magenta) using RNA *in situ* hybridization. (i) – (vii) indicate insets: individual channels are shown in gray scale to aid visualization (from left to right: *GABRP*, *SESN3*, *ISL1* and merge in (B), *ADAMTS18*, *SESN3*, *ISL1* in (C)), and dotted lines indicate a layer of amniotic epithelium and mesenchyme. Most amnion cells are positive for *GABRP*, *SESN3* and *ISL1*. *ADAMTS18* expression is restricted to a fraction of cells. In (iv), there are four *ADAMTS18*^{high} cells, while *ADAMTS18* is largely undetected in the amnion in (v). In (vi) and (vii), most cells are *ADAMTS18*^{high}. Fig. S3E provides a bird's-eye view of the CS12/13 embryo sample in (B) in which uterus and placenta are readily seen.
FB; forebrain, HB, hindbrain; FG, foregut; C; cardiac tissue; NT, neural tube; S, somite.
* indicates an *ISL1*$^{+}$ tissue that is likely of genital tubercle lineage. Scale bars = 500μm.

Figure 3. CLDN10 is an AmP marker expressed in the amnion-epiblast boundary cells of the PASE model as well as cynomolgus macaque peri-gastrula

(A) A dotplot of selected AmP markers.

(B) Expression of *CLDN10* superimposed onto the d3 hPSC-amnion as well as in Tyser *et al.* CS7 human embryo UMAP plots.

(C) Confocal micrographs of developing hPSC-amnion harvested at indicated timepoints, stained with indicated markers. A white arrowhead indicates a CLDN10/TFAP2A double-positive cell. CLDN10 expression is extinguished by d4. Membrane was stained using wheat germ agglutinin.

(D) Optical sections of PASE stained with indicated markers. White arrowheads indicate CLDN10 staining at the amnion-epiblast boundary.

(E,F) Confocal images of cynomolgus macaque embryos staged at CS6/7 (E) and CS7 (F) stained using indicated markers. CLDN10 is expressed at the transitioning boundary cells between the amnion and the epiblast. Insets indicate magnified regions. White arrowheads in (F – ii) indicate selected boundary cells with membrane CLDN10 staining. Clear membrane CLDN10 staining is not detected on the anterior side of the boundary cells (F – iii). Fig. S4H provides a bird's-eye view of the CS7 embryo in (F) with uterus and placental tissues. Scale bars = 20μm (C,D), 200μm (E), 500μm (F).

Figure 4. CLDN10 labels the amnion-epiblast boundary cells of cynomolgus macaque embryos undergoing the initial stages of organogenesis

(A-D) Confocal images of cynomolgus macaque embryos staged at CS8 (A,B) and CS9 (C,D) stained using indicated markers. Insets indicate magnified regions. CLDN10 is expressed at the anterior and posterior amnion-embryo boundaries in the CS8 embryo displaying the head-fold formation (A,B). The anterior head-fold region is magnified in (ii in (A) and (B)). White arrowheads indicate a squamous cell with a clear membrane CLDN10 staining (A - i). Brackets in (A) and (B) indicate regions with membrane CLDN10 staining. In the CS9 embryo (early organogenesis stage in (C) and (D)), while some posterior boundary CLDN10 staining is seen (seen in (iii)), the anterior CLDN10 staining is highly prominent at the amnion-anterior surface ectoderm border (in (i)). CLDN10 is also enriched in the dorsal foregut labeled by ISL1/2 and SOX2 but not SOX17 (indicated by * in (ii)). Fig. S4I and S4J provide bird's-eye views of the CS8 ((A) and (B)) and CS9 ((C) and (D)) embryos. HT, heat tube; FB, forebrain; YS, yolk sac. White arrowheads indicate the foregut pocket, while white arrows indicate the hindgut pocket. Bracket indicates somites in (C) and (D). Scale bars = 200μm (A,B), 500μm (C,D).

Figure S1.

(A) A UMAP plot displaying the single cell transcriptomes of 379 d3 hPSC-amnion cells with two identified clusters (AmP – sage color; advAm – salmon color).

(B) Predicted cell cycle (default parameter in Seurat) superimposed onto the d3 amnion UMAP plot.

(C) Venn diagrams showing a fraction of G1, G2/M or S cells in AmP (left) and advAm (right).

Figure S2.

547 (A) A UMAP plot displaying the original single cell transcriptome coordinates of the CS7
548 human embryo described in Tyser *et al.*, shown with the original annotations.
549 (B,C) Expression of indicated *pan*-amnion (B) and late/advanced amnion (C) markers
550 superimposed onto the UMAP plot.
551
552 **Figure S3.**
553 (A,B) UMAP plots displaying the Tyser *et al.* CS7 human embryo and d3 hPSC-amnion
554 single cell RNA sequencing integrated dataset (cell annotations shown in A, and sample
555 type annotations shown in B)
556 (C,D) Expression of indicated *pan*-amnion (C) and late/advanced amnion (D) markers
557 superimposed onto the UMAP plot.
558 (E) An overview image of the CS12/13 embryo implantation site shown in Fig. 2B. Only
559 nuclear staining is shown in grayscale. Scale bar = 2mm.
560
561 **Figure S4.**
562 (A) Expression of CLDN10 superimposed onto the uncropped Tyser *et al.* CS7 human
563 embryo UMAP plot.
564 (B) A UMAP plot displaying the GD14 cynomolgus macaque single cell transcriptome
565 with six identified general clusters (epiblast light blue; transition – purple; amnion – gold;
566 mesoderm – green; endoderm – teal; extraembryonic mesoderm – salmon). Arrow
567 indicates the likely trajectory of amnion differentiation based on the data in Yang *et al.*
568 as well as the expression analysis in (C). Note that, although not identical to the
569 published UMAP plot in Yang *et al.*, general characteristics are well recapitulated.
570 Trophectoderm cells have been omitted as performed in Yang *et al.*.
571 (C) Expression of indicated markers superimposed onto the Yang *et al.* UMAP plot.
572 Advanced amnion markers (EPAS1 and GABRP) are expressed at the tip of the
573 TFAP2A and ISL1 double-positive amnion cluster. CLDN10 positive cells show a weak
574 TBXT expression level.
575 (D,E) Individual channels of the whole embryo images in Fig. 4A and 4B, respectively.
576 (F,G) Individual channels of the whole embryo images in Fig. 4C and 4D, respectively.
577 (H-J) Overview images of the CS7 (H, from Fig. 3F), CS8 (I, Fig. 4A) and CS9 (J, Fig.
578 4C) embryo implantation sites (DNA signal shown in gray scale, Scale bar = 2mm).
579
580 **Table 1. Lists of differentially expressed genes in AmP (493) and advAm (563)**
581 **clusters**
582
583 **Table 2. List of antibodies and RNAscope probes used in this study**
584
585 **ACKNOWLEDGEMENTS**
586 We thank the Wisconsin National Primate Research Center (WNPRC) Veterinary,
587 Scientific Protocol Implementation, Pathology and Animal Services staff for providing
588 animal care, and assisting in procedures including breeding, pregnancy monitoring, and
589 sample collection. The contents of this manuscript are solely the responsibility of the
590 authors and do not represent the official views of the NIH.
591 **Funding:** This work was supported by NIH grants R01-HD098231, R01-DK089933,
592 P51 OD011106 (to the WNPRC) as well as by MCW CBNA Start-up funds. Specifically,

R01-DK089933 and MCW CBNA Start-up funds were used to perform experiments using PASE. **Competing interests:** The authors declare no competing interest. **Data and materials availability**: All data needed to evaluate the conclusions in the paper are present in the paper and the Supplementary Materials. The raw data, unfiltered count matrix and processed count matrix will be available to the database of Genotypes and Phenotypes (dbGaP) upon publication. Further information and requests for reagents may be directed to Kenichiro Taniguchi.

REFERENCES

Anderson, R.M., Lawrence, A.R., Stottmann, R.W., Bachiller, D., and Klingensmith, J. (2002). Chordin and noggin promote organizing centers of forebrain development in the mouse. Development *129*, 4975-4987.

Angelow, S., Ahlstrom, R., and Yu, A.S. (2008). Biology of claudins. Am J Physiol Renal Physiol *295*, F867-876.

Arnold, S.J., and Robertson, E.J. (2009). Making a commitment: cell lineage allocation and axis patterning in the early mouse embryo. Nature reviews Molecular cell biology *10*, 91-103.

Bergen, V., Lange, M., Peidli, S., Wolf, F.A., and Theis, F.J. (2020). Generalizing RNA velocity to transient cell states through dynamical modeling. Nature biotechnology *38*, 1408-1414.

Bergmann, S., Penfold, C.A., Slatery, E., Siriwardena, D., Drummer, C., Clark, S., Strawbridge, S.E., Kishimoto, K., Vickers, A., Tewary, M.*, et al.* (2022). Spatial profiling of early primate gastrulation in utero. Nature *609*, 136-143.

Butler, A., Hoffman, P., Smibert, P., Papalexi, E., and Satija, R. (2018). Integrating single-cell transcriptomic data across different conditions, technologies, and species. Nature biotechnology *36*, 411-420.

Cao, J., Spielmann, M., Qiu, X., Huang, X., Ibrahim, D.M., Hill, A.J., Zhang, F., Mundlos, S., Christiansen, L., Steemers, F.J.*, et al.* (2019). The single-cell transcriptional landscape of mammalian organogenesis. Nature *566*, 496-502.

Carleton, A.E., Duncan, M.C., and Taniguchi, K. (2022). Human epiblast lumenogenesis: From a cell aggregate to a lumenal cyst. Seminars in cell & developmental biology *131*, 117-123.

Chen, K., Zheng, Y., Xue, X., Liu, Y., Resto Irizarry, A.M., Tang, H., and Fu, J. (2021). Branching development of early post-implantation human embryonic-like tissues in 3D stem cell culture. Biomaterials *275*, 120898.

Dobreva, M.P., Lhoest, L., Pereira, P.N., Umans, L., Camus, A., Chuva de Sousa Lopes, S.M., and Zwijsen, A. (2012). Periostin as a biomarker of the amniotic membrane. Stem Cells Int *2012*, 987185.

Enders, A.C., Hendrickx, A.G., and Schlafke, S. (1983). Implantation in the rhesus monkey: initial penetration of endometrium. The American journal of anatomy *167*, 275-298.

Enders, A.C., Schlafke, S., and Hendrickx, A.G. (1986). Differentiation of the embryonic disc, amnion, and yolk sac in the rhesus monkey. The American journal of anatomy *177*, 161-185.

Geng, X., and Oliver, G. (2009). Pathogenesis of holoprosencephaly. J Clin Invest *119*, 1403-1413.

Hamed, M.M., Taniguchi, K., and Duncan, M.C. (2023). Monitoring Effects of Membrane Traffic Via Changes in Cell Polarity and Morphogenesis in Three-Dimensional Human Pluripotent Stem Cell Cysts. Methods in molecular biology *2557*, 83-98.

Hao, Y., Hao, S., Andersen-Nissen, E., Mauck, W.M., 3rd, Zheng, S., Butler, A., Lee, M.J., Wilk, A.J., Darby, C., Zager, M.*, et al.* (2021). Integrated analysis of multimodal single-cell data. Cell *184*, 3573-3587 e3529.

La Manno, G., Soldatov, R., Zeisel, A., Braun, E., Hochgerner, H., Petukhov, V., Lidschreiber, K., Kastriti, M.E., Lonnerberg, P., Furlan, A.*, et al.* (2018). RNA velocity of single cells. Nature *560*, 494-498.

Miki, T., Lehmann, T., Cai, H., Stolz, D.B., and Strom, S.C. (2005). Stem cell characteristics of amniotic epithelial cells. Stem cells *23*, 1549-1559.

Muenke, M., and Beachy, P.A. (2000). Genetics of ventral forebrain development and holoprosencephaly. Current opinion in genetics & development *10*, 262-269.

Nakamura, T., Okamoto, I., Sasaki, K., Yabuta, Y., Iwatani, C., Tsuchiya, H., Seita, Y., Nakamura, S., Yamamoto, T., and Saitou, M. (2016). A developmental coordinate of pluripotency among mice, monkeys and humans. Nature *537*, 57-62.

Nakamura, T., Yabuta, Y., Okamoto, I., Sasaki, K., Iwatani, C., Tsuchiya, H., and Saitou, M. (2017). Single-cell transcriptome of early embryos and cultured embryonic stem cells of cynomolgus monkeys. Scientific data *4*, 170067.

Nishioka, N., Nagano, S., Nakayama, R., Kiyonari, H., Ijiri, T., Taniguchi, K., Shawlot, W., Hayashizaki, Y., Westphal, H., Behringer, R.R.*, et al.* (2005). Ssdp1 regulates head morphogenesis of mouse embryos by activating the Lim1-Ldb1 complex. Development *132*, 2535-2546.

Overeem, A.W., Chang, Y.W., Moustakas, I., Roelse, C.M., Hillenius, S., Helm, T.V., Schrier, V.F.V., Goncalves, M., Mei, H., Freund, C.*, et al.* (2023). Efficient and scalable generation of primordial germ cells in 2D culture using basement membrane extract overlay. Cell Rep Methods *3*, 100488.

Roost, M.S., van Iperen, L., Ariyurek, Y., Buermans, H.P., Arindrarto, W., Devalla, H.D., Passier, R., Mummery, C.L., Carlotti, F., de Koning, E.J.*, et al.* (2015). KeyGenes, a Tool to Probe Tissue Differentiation Using a Human Fetal Transcriptional Atlas. Stem cell reports *4*, 1112-1124.

Sasaki, K., Nakamura, T., Okamoto, I., Yabuta, Y., Iwatani, C., Tsuchiya, H., Seita, Y., Nakamura, S., Shiraki, N., Takakuwa, T.*, et al.* (2016). The Germ Cell Fate of Cynomolgus Monkeys Is Specified in the Nascent Amnion. Developmental cell *39*, 169-185.

Sekulovski, N., Wettstein, J.C., Carleton, A.E., Taniguchi, L.E., Ma, X., Rao, S., Schmidt, J.K., Golos, T.G., Lin, C.-W., and Taniguchi, K. (2023). Temporally resolved early BMP-driven transcriptional cascade during human amnion specification. eLife *12: RP89367*.

Shahbazi, M.N., and Zernicka-Goetz, M. (2018). Deconstructing and reconstructing the mouse and human early embryo. Nature cell biology.

Shao, Y., and Fu, J. (2022). Engineering multiscale structural orders for high-fidelity embryoids and organoids. Cell stem cell *29*, 722-743.

Shao, Y., Taniguchi, K., Gurdziel, K., Townshend, R.F., Xue, X., Yong, K.M.A., Sang, J., Spence, J.R., Gumucio, D.L., and Fu, J. (2017a). Self-organized amniogenesis by

human pluripotent stem cells in a biomimetic implantation-like niche. Nature materials *16*, 419-425.
Shao, Y., Taniguchi, K., Townshend, R.F., Miki, T., Gumucio, D.L., and Fu, J. (2017b). A pluripotent stem cell-based model for post-implantation human amniotic sac development. Nature communications *8*, 208.
Shawlot, W., Wakamiya, M., Kwan, K.M., Kania, A., Jessell, T.M., and Behringer, R.R. (1999). Lim1 is required in both primitive streak-derived tissues and visceral endoderm for head formation in the mouse. Development *126*, 4925-4932.
Taniguchi, K., Heemskerk, I., and Gumucio, D.L. (2019). Opening the black box: Stem cell-based modeling of human post-implantation development. The Journal of cell biology *218*, 410-421.
Taniguchi, K., Shao, Y., Townshend, R.F., Tsai, Y.H., DeLong, C.J., Lopez, S.A., Gayen, S., Freddo, A.M., Chue, D.J., Thomas, D.J.*, et al.* (2015). Lumen Formation Is an Intrinsic Property of Isolated Human Pluripotent Stem Cells. Stem cell reports *5*, 954-962.
Ton, M.N., Keitley, D., Theeuwes, B., Guibentif, C., Ahnfelt-Ronne, J., Andreassen, T.K., Calero-Nieto, F.J., Imaz-Rosshandler, I., Pijuan-Sala, B., Nichols, J.*, et al.* (2023). An atlas of rabbit development as a model for single-cell comparative genomics. Nature cell biology *25*, 1061-1072.
Townshend, R.F., Shao, Y., Wang, S., Cortez, C.L., Esfahani, S.N., Spence, J.R., O'Shea, K.S., Fu, J., Gumucio, D.L., and Taniguchi, K. (2020). Effect of Cell Spreading on Rosette Formation by Human Pluripotent Stem Cell-Derived Neural Progenitor Cells. Front Cell Dev Biol *8*, 588941.
Tyser, R.C.V., Mahammadov, E., Nakanoh, S., Vallier, L., Scialdone, A., and Srinivas, S. (2021). Single-cell transcriptomic characterization of a gastrulating human embryo. Nature *600*, 285-289.
Yang, R., Goedel, A., Kang, Y., Si, C., Chu, C., Zheng, Y., Chen, Z., Gruber, P.J., Xiao, Y., Zhou, C.*, et al.* (2021). Amnion signals are essential for mesoderm formation in primates. Nature communications *12*, 5126.
Yang, Y.P., Anderson, R.M., and Klingensmith, J. (2010). BMP antagonism protects Nodal signaling in the gastrula to promote the tissue interactions underlying mammalian forebrain and craniofacial patterning. Hum Mol Genet *19*, 3030-3042.
Zhao, C., Reyes, A.P., Schell, J.P., Weltner, J., Ortega, N.M., Zheng, Y., Björklund, Å.K., Rossant, J., Fu, J., Petropoulos, S.*, et al.* (2021). Reprogrammed blastoids contain amnion-like cells but not trophectoderm. bioRxiv, 2021.2005.2007.442980.
Zheng, Y., Xue, X., Shao, Y., Wang, S., Esfahani, S.N., Li, Z., Muncie, J.M., Lakins, J.N., Weaver, V.M., Gumucio, D.L.*, et al.* (2019). Controlled modelling of human epiblast and amnion development using stem cells. Nature *573*, 421-425.
Zheng, Y., Yan, R.Z., Sun, S., Kobayashi, M., Xiang, L., Yang, R., Goedel, A., Kang, Y., Xue, X., Esfahani, S.N.*, et al.* (2022). Single-cell analysis of embryoids reveals lineage diversification roadmaps of early human development. Cell stem cell *29*, 1402-1419 e1408.

Figure 1

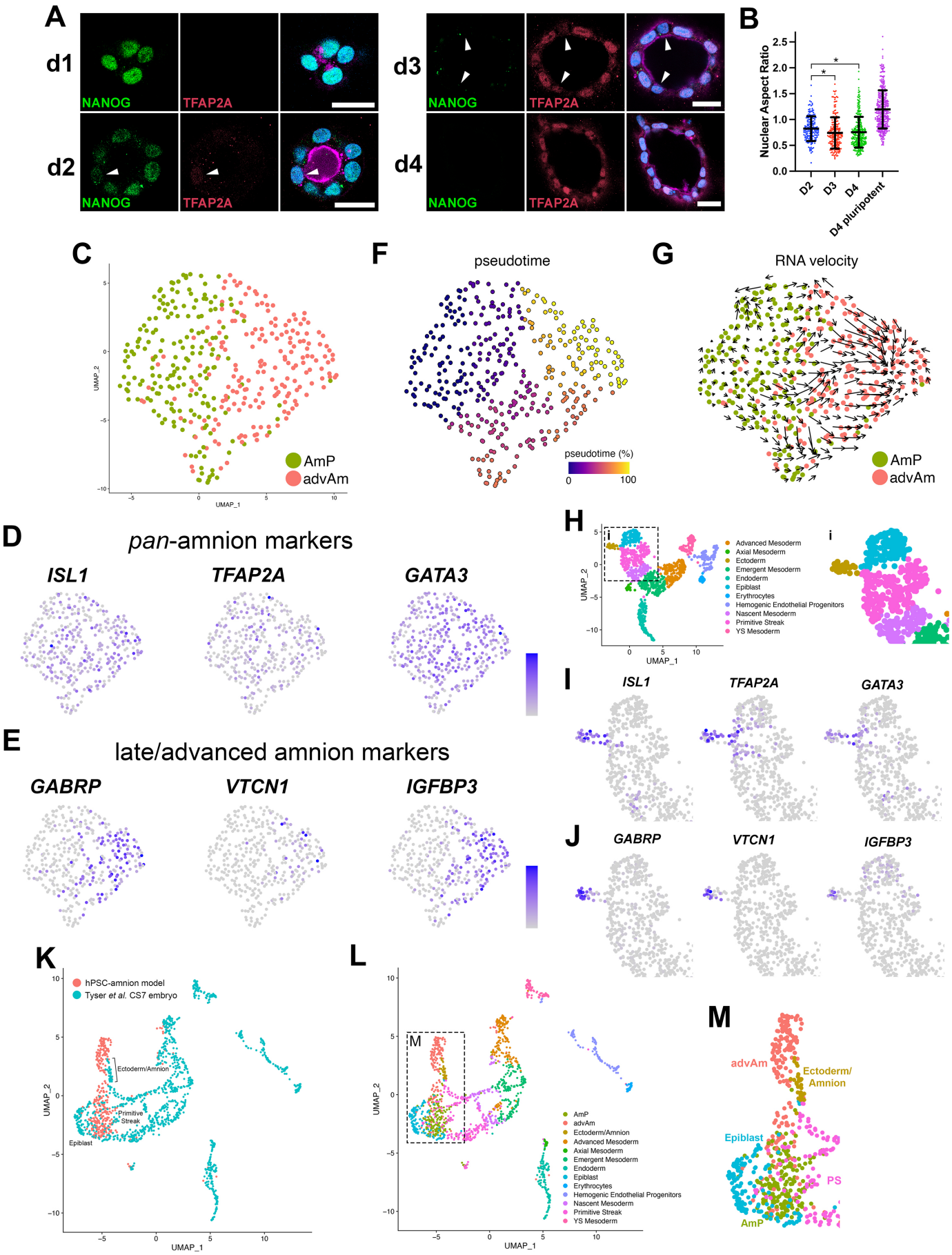
A
d1
d2
d3
d4
NANOG
TFAP2A
B
Nuclear Aspect Ratio
D2
D3
D4
D4 pluripotent
C
UMAP_1
UMAP_2
AmP
advAm
F
pseudotime
pseudotime (%)
0
100
G
RNA velocity
AmP
advAm
D
pan-amnion markers
ISL1
TFAP2A
GATA3
E
late/advanced amnion markers
GABRP
VTCN1
IGFBP3
H
Advanced Mesoderm
Axial Mesoderm
Ectoderm
Emergent Mesoderm
Endoderm
Epiblast
Erythrocytes
Hemogenic Endothelial Progenitors
Nascent Mesoderm
Primitive Streak
YS Mesoderm
I
ISL1
TFAP2A
GATA3
J
GABRP
VTCN1
IGFBP3
K
hPSC-amnion model
Tyser et al. CS7 embryo
Ectoderm/Amnion
Primitive Streak
Epiblast
L
M
advAm
Ectoderm/ Amnion
Epiblast
PS
AmP

Figure 2

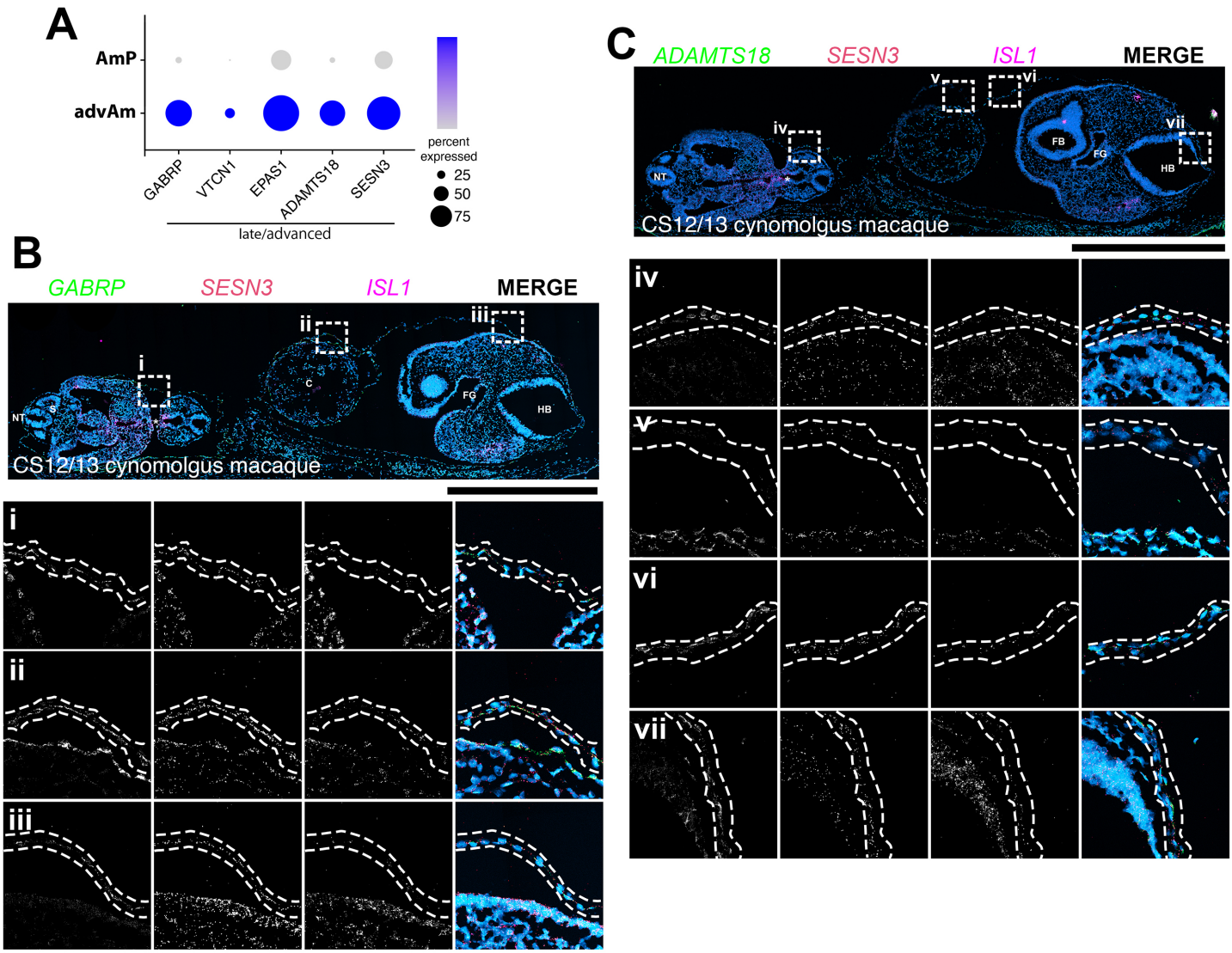
A
AmP
advAm
GABRP
VTCN1
EPAS1
ADAMTS18
SESN3
late/advanced
percent expressed
25
50
75
B
GABRP
SESN3
ISL1
MERGE
i
ii
iii
NT
S
C
FG
HB
CS12/13 cynomolgus macaque
C
ADAMTS18
SESN3
ISL1
MERGE
iv
v
vi
vii
NT
FB
FG
HB
CS12/13 cynomolgus macaque

Figure 3

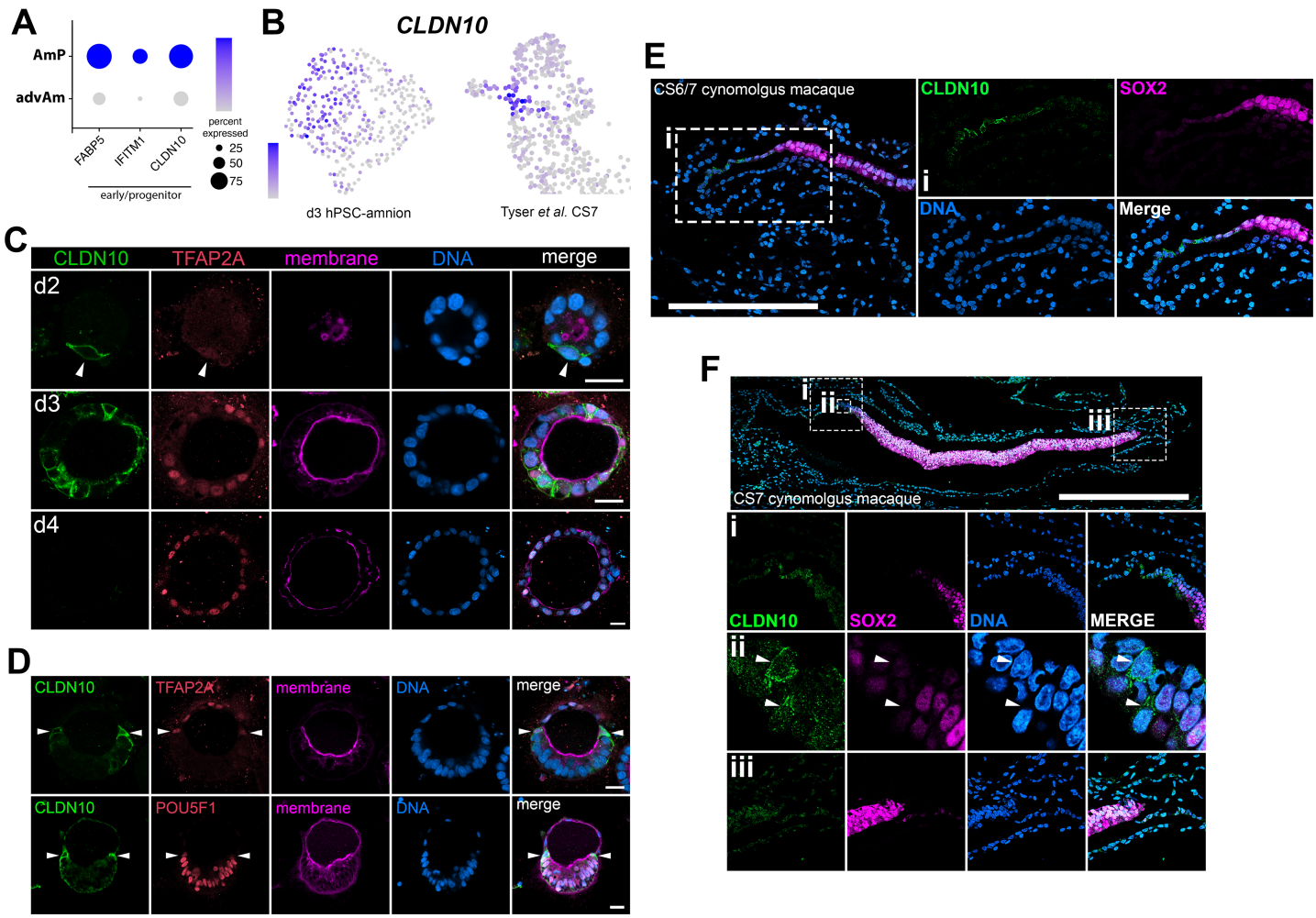
A
AmP
advAm
FABP5
IFITM1
CLDN10
early/progenitor
percent expressed
25
50
75
B
CLDN10
d3 hPSC-amnion
Tyser et al. CS7
C
CLDN10
TFAP2A
membrane
DNA
merge
d2
d3
d4
D
CLDN10
TFAP2A
membrane
DNA
merge
CLDN10
POU5F1
membrane
DNA
merge
E
CS6/7 cynomolgus macaque
i
CLDN10
SOX2
DNA
Merge
F
i
ii
iii
CS7 cynomolgus macaque
CLDN10
SOX2
DNA
MERGE

Figure 4

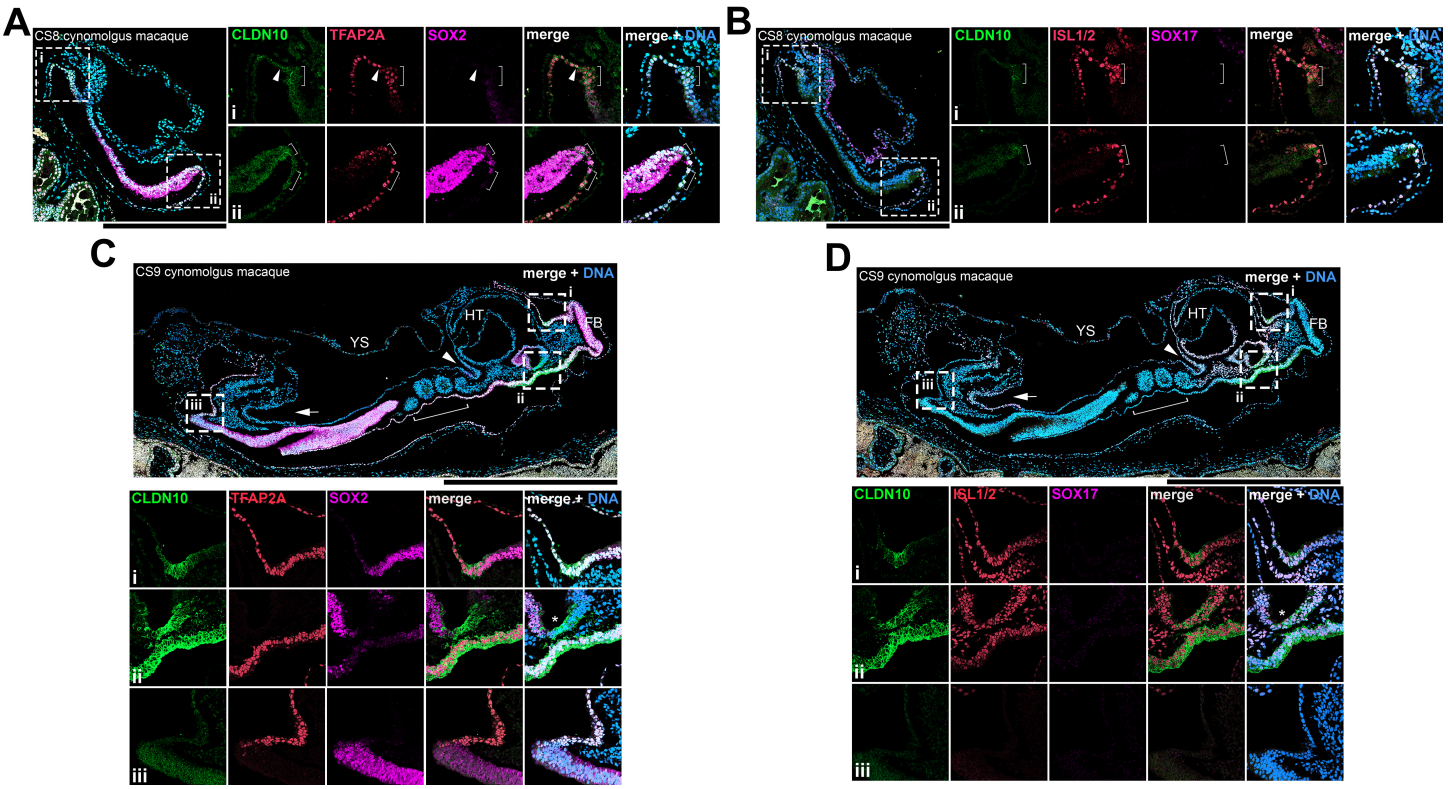
A
CS8 cynomolgus macaque
CLDN10
TFAP2A
SOX2
merge
merge + DNA
B
CS8 cynomolgus macaque
CLDN10
ISL1/2
SOX17
merge
merge + DNA
C
CS9 cynomolgus macaque
merge + DNA
YS
HT
FB
CLDN10
TFAP2A
SOX2
merge
merge + DNA
D
CS9 cynomolgus macaque
merge + DNA
YS
HT
FB
CLDN10
ISL1/2
SOX17
merge
merge + DNA